eLIFE elifesciences.org

RESEARCH ARTICLE

Figures and figure supplements

The synaptic ribbon is critical for sound encoding at high rates and with temporal precision

Philippe Jean *et al*

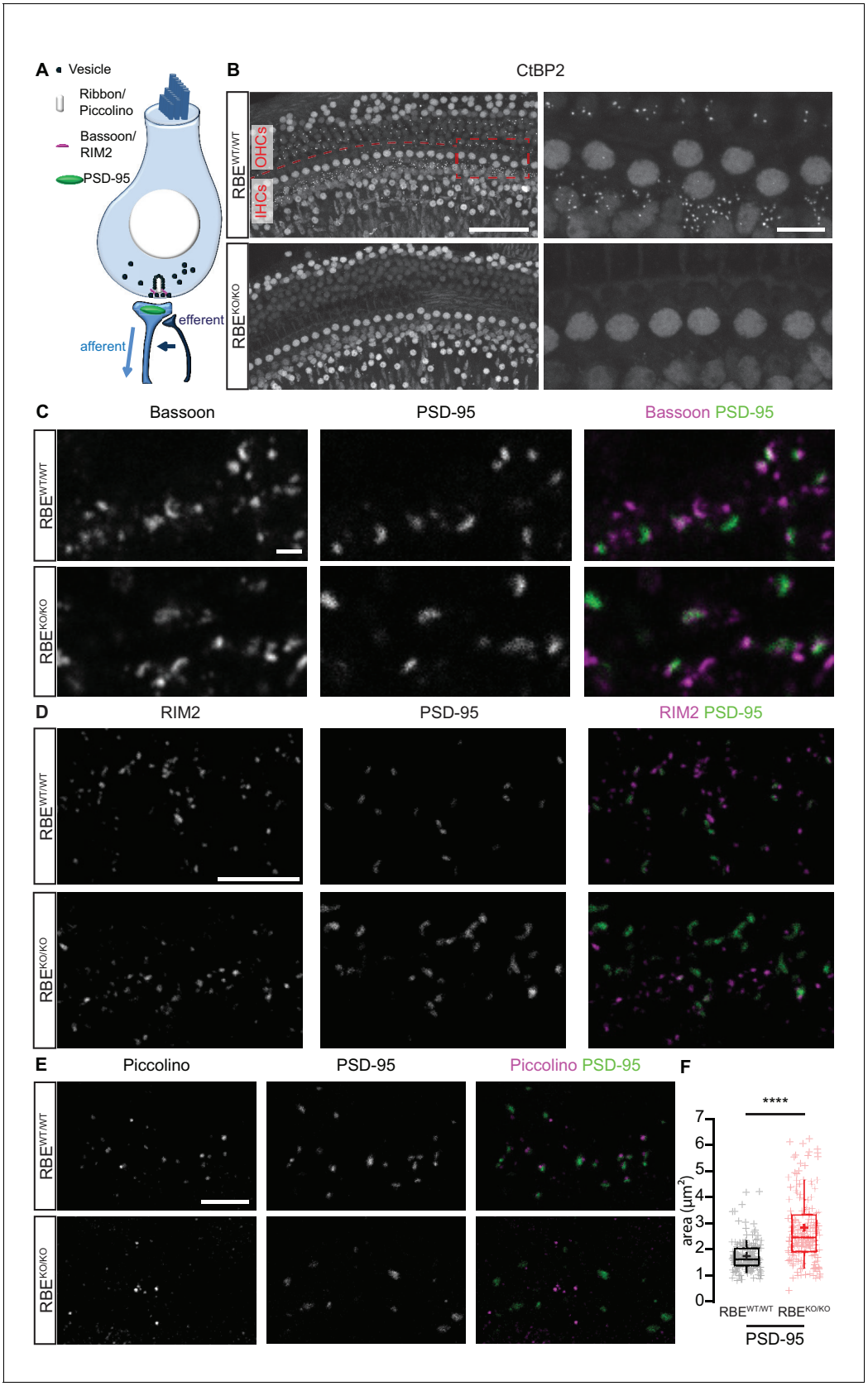

Figure 1. Loss of synaptic ribbons and piccolino from the AZs of RIBEYE-deficient IHCs. (**A**) Simplified schematic representation of an IHC with the afferent and efferent connectivities. (**B**) Maximal projection of confocal sections from organs of Corti immunolabeled for CtBP2 and RIBEYE, present in

Figure 1 continued on next page

Figure 1 continued

the nuclei and the ribbons, respectively. The $RBE^{WT/WT}$ staining (top row) shows small puncta in the outer hair cell (OHC) and IHC rows representing the synaptic ribbons, which are completely absent in the $RBE^{KO/KO}$ hair cells (bottom row). Scale bar = 50 µm. Zoom into the IHC row (right column), emphasizes the complete disappearance of CtBP2-labeling at the basolateral part of $RBE^{KO/KO}$ IHCs. Scale bar = 10 µm. (**C**) Maximal projection of confocal sections from organs of Corti co-labeled for the presynaptic marker and anchor of the ribbon, bassoon (left column), and the postsynaptic marker, PSD-95 (middle column), in $RBE^{WT/WT}$ and $RBE^{KO/KO}$ IHCs. The merged picture (right column) shows the juxtaposition of bassoon (magenta) with PSD-95 (green), indicating its presence both at $RBE^{WT/WT}$ and ribbonless $RBE^{KO/KO}$ IHC synapses. Scale bar = 1 µm. (**D**) Maximal projection of confocal sections from organs of Corti co-labeled for the presynaptic marker RIM2 (left column) and the postsynaptic marker PSD-95 (middle column). The merged picture (right column) shows the co-localization of RIM2 (magenta) with PSD-95 (green) meaning its presence at the ribbonless IHC pre-synapses (scale bar = 5 µm). (**E**) Maximal projection of confocal sections from organs of Corti co-labeled for piccolino, a specific short splice variant of piccolo found at ribbons of $RBE^{WT/WT}$ IHC synapses (left column), co-labeled with PSD-95 (middle column). The merged pictures (right column) show PSD-95 (green) immunofluorescence lacking juxtaposed piccolino signal (magenta) in $RBE^{KO/KO}$ (bottom row), indicating absence of piccolino from afferent synapses of mutant IHCs. The punctate labeling for piccolo, away from PSD-95, most likely represents labeling of piccolo at conventional efferent synapses (schematically shown in ***Figure 1A***). Scale bar = 5 µm. (**F**) Quantification of the area of PSD-95 immunofluorescent spots. The PSD-95 spots are siginificantly bigger in the $RBE^{KO/KO}$ IHCs ($p<0.0001$, Mann-Whitney-Wilcoxon test, $n = 178$ spots, N = 3 for $RBE^{KO/KO}$ and $n = 163$ spots, N = 3 for $RBE^{WT/WT}$). Box plots show 10, 25, 50, 75 and 90^{th} percentiles with individual data points overlaid; means are shown as crosses.

DOI: https://doi.org/10.7554/eLife.29275.003

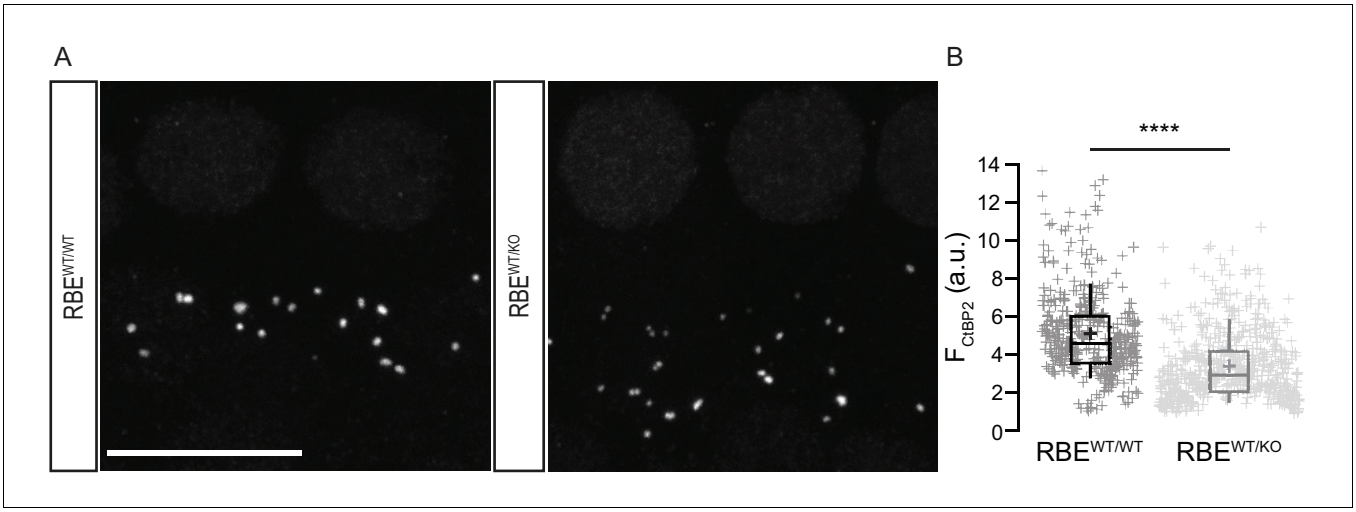

Figure 1—figure supplement 1. Gene-dosage dependent expression of the RIBEYE at IHC AZs. (**A**) Maximal projection of organs of Corti immunolabeled for the C-terminal domain of both CtBP2 and RIBEYE, present in the nuclei and the ribbons. The number of ribbons does not differ between $RBE^{WT/KO}$ (*n* = 50 IHCs, N = 4) and $RBE^{WT/WT}$ IHCs (*n* = 39 IHCs, N = 3). Scale bar = 10 µm. (**B**) Box plot highlighting significantly reduced immunofluorescence intensities for the ribbons in the heterozygous condition (*n* = 600 spots for 40 $RBE^{WT/KO}$ IHCs, N = 3 and *n* = 411 spots for 29 $RBE^{WT/WT}$ IHCs, N = 3, p<0.0001, Mann-Whitney-Wilcoxon test). Box plots show 10, 25, 50, 75 and 90th percentiles with individual immunofluorescent spots overlaid; means are shown as crosses.

DOI: https://doi.org/10.7554/eLife.29275.004

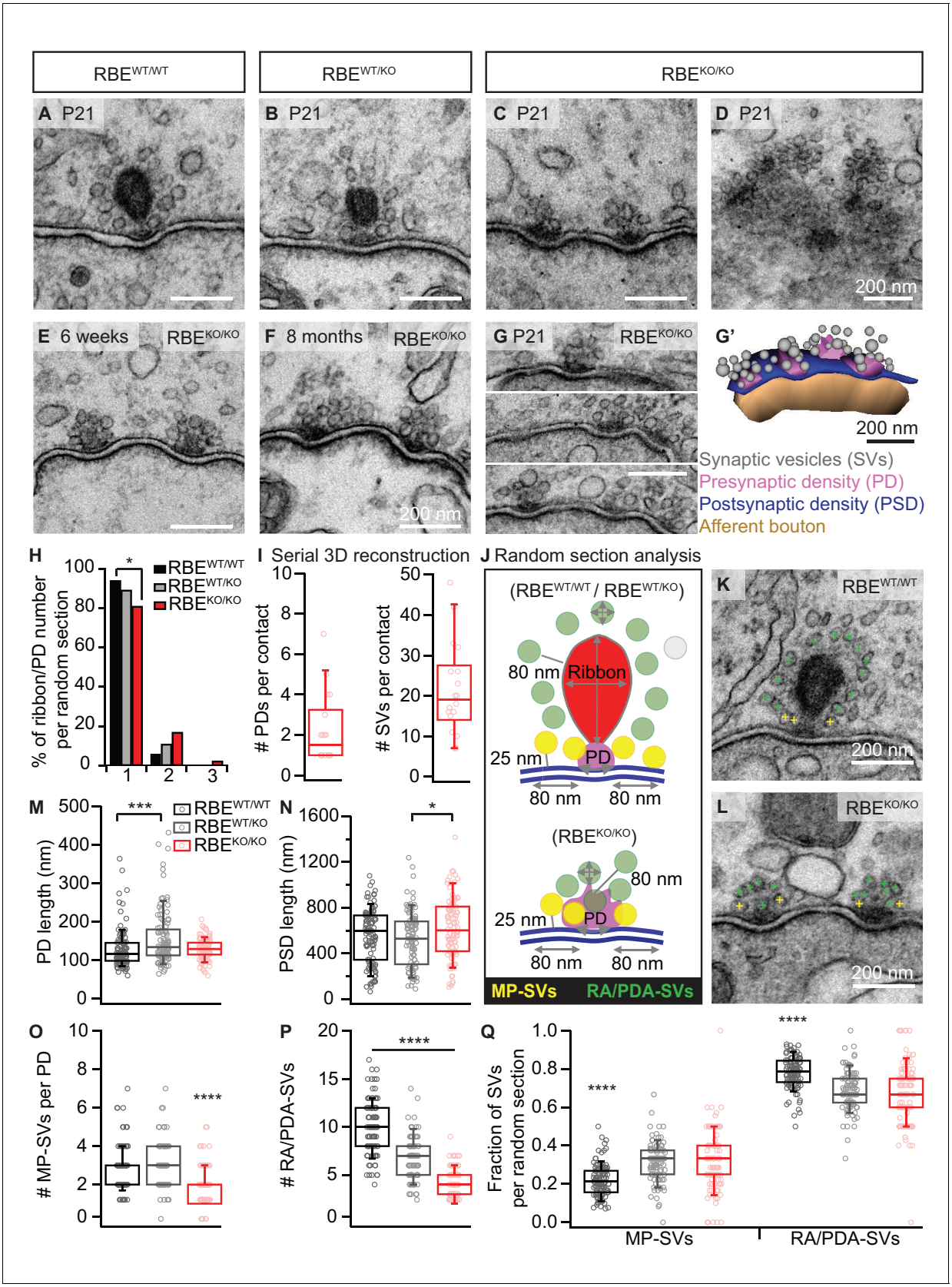

Figure 2. RIBEYE disruption transforms IHC synapses into contacts with multiple small ribbonless AZs. (**A–C**) Representative electron micrographs of IHC afferent synapses from P21 RBE$^{WT/WT}$, RBE$^{WT/KO}$ and RBE$^{KO/KO}$ mice. Ribbonless RBE$^{KO/KO}$ synapses display one or more presynaptic densities

Figure 2 continued on next page

Figure 2 continued

(PD) clustering SVs. Scale bars = 200 nm. (**D**) $RBE^{KO/KO}$ IHC AZ cut tangentially, revealing multiple PDs (here six) per AZ. (**E, F**) Representative electron micrographs of $RBE^{KO/KO}$ IHC synapses from mice at 6 weeks (**E**) and 8 months (**F**) of age: the presence of at least 2 AZs per contact in mature IHCs argues against a developmental delay. (**G**) Consecutive serial sections of a typical $RBE^{KO/KO}$ P21 IHC synapse showing multiple AZs. Scale bar = 200 nm. (**G'**) Corresponding serial 3D reconstruction of the synapse in (**G**) showing four PDs (magenta) surrounded by a total of 48 SVs (gray). Scale bar = 200 nm. (**H**) Quantification of the number of ribbon/PD per random section. AZs with a single PD are less frequently observed in $RBE^{KO/KO}$ IHCs (*n* = 108 AZs, N = 2 for $RBE^{KO/KO}$ and *n* = 106 AZs, N = 2 for $RBE^{WT/WT}$; p<0.05, NPMC test). (**I**) Number of PDs and SVs per AZ in P21 $RBE^{KO/KO}$ mice in serial 3D reconstructions of $RBE^{KO/KO}$ afferent synapses. Box plots show 10, 25, 50, 75 and 90th percentiles with individual data points overlaid, as for (M, N, O, P & Q). (**J**) Schematic drawing illustrating the quantitative analysis of random sections. SV diameter: average of vertical and horizontal measurements from outer rim to outer rim. The ribbon height, width and area were measured as indicated by the gray lines. The length of the PD was determined along the AZ. For ribbon-occupied AZs: Membrane-proximal (MP) SVs (yellow) were counted in a distance of ≤25 nm from the AZ membrane (blue) and ≤80 nm from the PD. Ribbon-associated (RA) SVs were found in the first layer around the ribbon (red) with a maximum distance of 80 nm to the ribbon, quantified as indicated by the gray lines. For ribbonless AZs: Instead of RA-SVs we defined PD-associated SVs (PDA-SVs: all SV at PD with a maximum distance of 80 nm to the PD not matching the MP-SV criteria, defined as above). (**K, L**) Electron micrographs illustrating the quantification of the MP-SVs (yellow crosses) and the RA/PDA-SVs (green crosses). (**M–Q**) Quantification of random IHC synapse (P_{21}) sections revealed no significant differences between RBE $^{KO/KO}$ and $RBE^{WT/WT}$ for the PD and PSD length (PD length: *n* = 108 PDs, N = 2 for RBE $^{KO/KO}$ and *n* = 108 PDs, N = 2 for $RBE^{WT/WT}$; p=0.92, NPMC test and PSD length: *n* = 98 PSDs, N = 2 for RBE $^{KO/KO}$ and *n* = 113 PSDs, N = 2 for $RBE^{WT/WT}$; p=0.11, Tukey's test). However, in the $RBE^{WT/KO}$ IHCs, the PDs were bigger than in the WT IHCs (*n* = 101 PDs, N = 2; p=0.0004, NPMC test), and the PSDs were smaller than in the knock-out IHCs (*n* = 100 PSDs, N = 2 for $RBE^{WT/KO}$; p=0.01, Tukey's test). MP-SVs (*n* = 108 AZs, N = 2 for $RBE^{KO/KO}$, *n* = 106 AZs, N = 2 for $RBE^{WT/WT}$; p<0.0001, NPMC test) and RA/PDA-SVs (*n* = 108 AZs, N = 2 for $RBE^{KO/KO}$, *n* = 106 AZs, N = 2 for $RBE^{WT/WT}$; p<0.0001, Tukey's test) per AZ, as well as the fraction of RA/PDA-SVs in $RBE^{KO/KO}$, were significantly reduced (*n* = 108 AZs, N = 2 for $RBE^{KO/KO}$, *n* = 106 AZs, N = 2 for $RBE^{WT/WT}$; p<0.0001, NPMC test).

DOI: https://doi.org/10.7554/eLife.29275.005

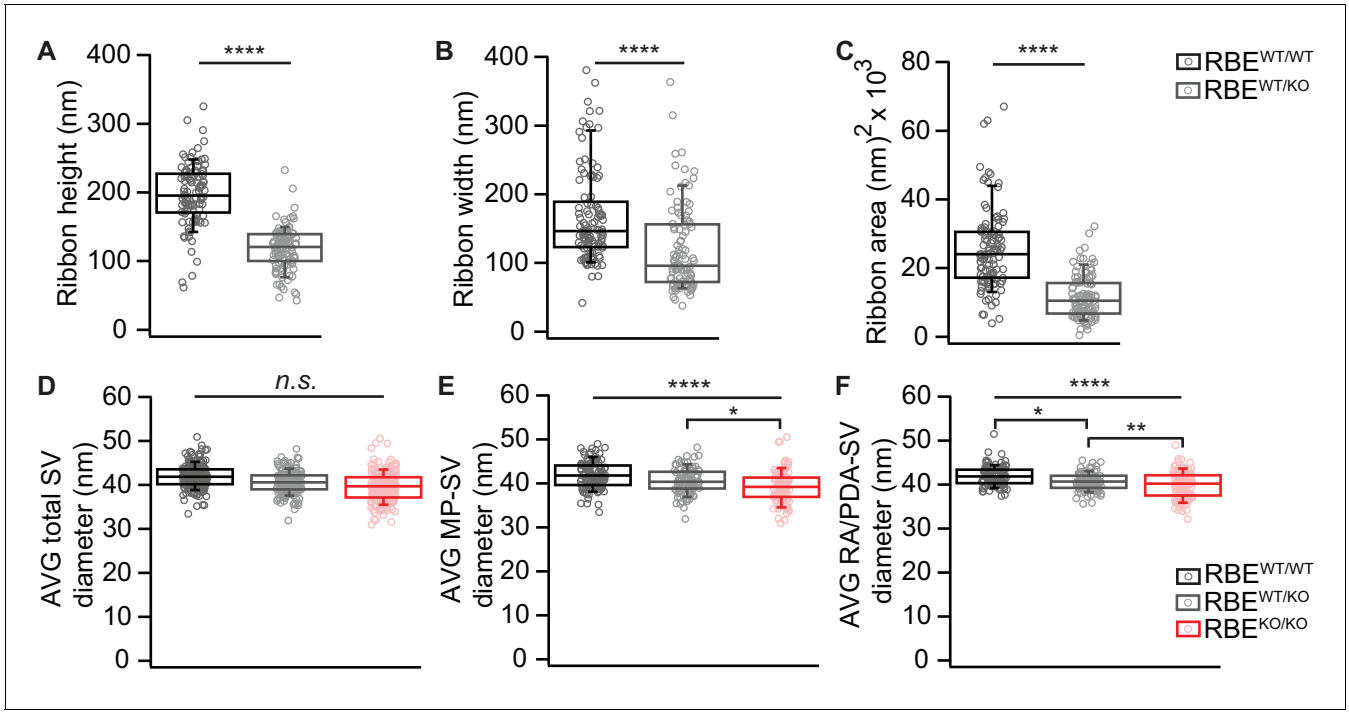

Figure 2—figure supplement 1. Random section analysis showed smaller synaptic ribbons and vesicles in $RBE^{WT/KO}$ mice. (**A–C**) Random section analysis of P21 mice revealed smaller ribbon sizes in $RBE^{WT/KO}$ IHCs (n = 101 ribbons, N = 2 for $RBE^{WT/KO}$, n = 106 ribbons, N = 2 for $RBE^{WT/WT}$; p<0.0001, Mann-Whitney-Wilcoxon test for all), while the SV diameter per ribbon/PD was unaltered for all three genotypes considering all SVs (**D**): n = 108 AZs, N = 2 for $RBE^{KO/KO}$, n = 101 AZs, N = 2 for $RBE^{WT/KO}$, n = 106 AZs, N = 2 for $RBE^{WT/WT}$ as for (**E, F**); p=0.30, NPMC test. However, a reduction of MP-SV diameter (**E**): $RBE^{KO/KO}$ and $RBE^{WT/KO}$ vs. $RBE^{WT/WT}$; p<0.0001, NPMC test and $RBE^{WT/KO}$ vs. $RBE^{KO/KO}$; p=0.03, NPMC test) and RA/PDA-SV diameter (**F**): $RBE^{KO/KO}$, vs. $RBE^{WT/WT}$; p<0.0001, NPMC test and $RBE^{KO/KO}$ vs. $RBE^{WT/KO}$; p=0.003, NPMC test and $RBE^{WT/KO}$ vs. $RBE^{WT/WT}$; p=0.02, NPMC test) was observed for $RBE^{WT/KO}$ and $RBE^{KO/KO}$. Box plots show 10, 25, 50, 75 and 90th percentiles with individual data points overlaid.
DOI: https://doi.org/10.7554/eLife.29275.006

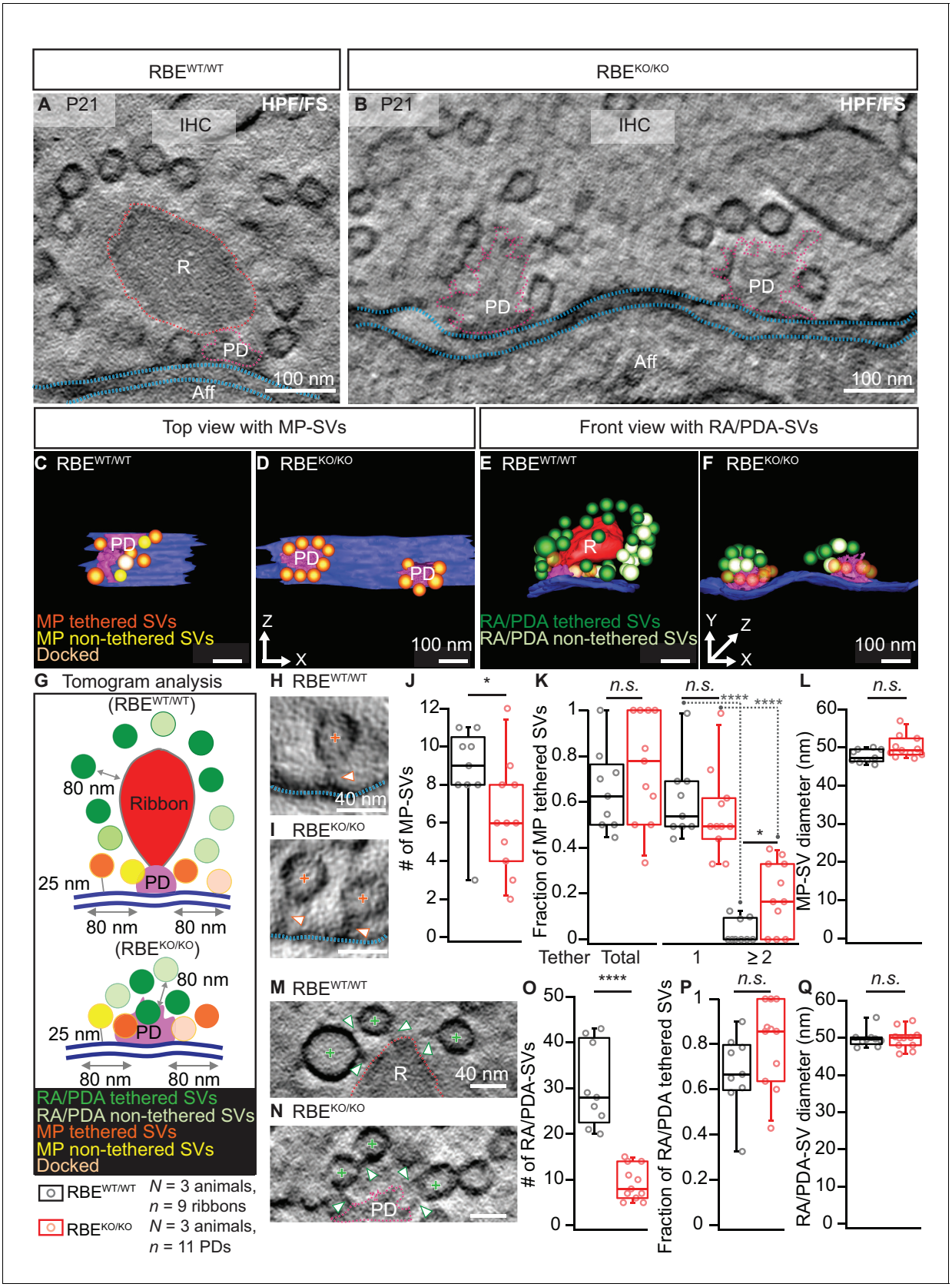

Figure 3. Electron tomography analysis of synaptic ultrastructure obtained after HPF/FS. (**A, B**) Exemplary virtual electron tomographic sections of P21 RBE$^{WT/WT}$ (**A**) and RBE$^{KO/KO}$ (**B**) highlight the ribbon R in red, the presynaptic density (PD) in magenta and the AZ membrane with blue dotted lines. No

Figure 3 continued on next page

Figure 3 continued

synaptic ribbons, but two PDs were observed in $RBE^{KO/KO}$ (**B**). Scale bars = 100 nm. (**C–F**) 3D rendered models of $RBE^{WT/WT}$ (**C, E**) and $RBE^{KO/KO}$ (**D, F**) IHC synapses. (**C, D**) The top view depicts the MP-SV pool with tethered (orange), non-tethered (yellow) and docked (light orange) SVs. For clarity ribbons, RA/PDA-SVs are removed. Scale bars = 100 nm. (**E,F**) The front view shows the RA/PDA-SV pool from $RBE^{WT/WT}$ (**E**) and $RBE^{KO/KO}$ (**F**) IHCs. Tethered (dark green) and non-tethered (light green) RA/PDA-SVs. For the ease of visualization, the MP-SV pool is transparent here and other synaptic structures such as ribbon (red), PD (magenta) and AZ membrane (blue) are indicated. Scale bars = 100 nm. (**G**) Illustrations show the tomogram analysis parameters comparable to 2D-random section analysis (***Figure 2***), in addition to that the vesicle pools are subdivided into tethered, non-tethered and docked SVs. (**H, I, M, N**) Representative tomogram virtual sections of membrane-tethered MP-SVs (H, I; orange cross), ribbon/PD tethered SVs and ribbon/PD proximal interconnecting SVs (M, N; green cross) in $RBE^{WT/WT}$ (**H, M**) and in $RBE^{KO/KO}$ (**I, N**). Tethers are marked with a white arrowhead and other synaptic entities are color-coded similar to (**A, B**). Scale bars = 40 nm. (**J–L**) Quantification for the MP-SV pool is depicted; n = 9 ribbons, N = 3 animals for $RBE^{WT/WT}$ and n = 11 PDs, N = 3 animals for $RBE^{KO/KO}$. Fewer MP-SV were observed in $RBE^{KO/KO}$ (J; p=0.04, Mann-Whitney-Wilcoxon test). The fraction of tethered MP-SVs was unaltered in $RBE^{KO/KO}$ (K; p=0.30, t-test). Most of the SVs were tethered by a single tether in both $RBE^{KO/KO}$ and $RBE^{WT/WT}$. Significantly more SVs with multiple-tethers were observed in $RBE^{KO/KO}$ (K; single tethered MP-SVs, multiple-tethered MP-SVs: n.s.: p>0.05,*: p=0.01, ****: p<0.0001, Tukey's test). MP-SV diameter was unaltered in $RBE^{KO/KO}$ (L; p=0.06, Mann-Whitney-Wilcoxon test). (**O–Q**) Quantification for the RA/PDA-SVs, sample size is same as for the MP-SV analysis. Significantly fewer PDA-SVs were observed in $RBE^{KO/KO}$ (O; $RBE^{KO/KO}$: p<0.0001, Mann-Whitney-Wilcoxon test). The fraction of PDA tethered SVs in $RBE^{KO/KO}$ was comparable to RA tethered SVs in $RBE^{WT/WT}$ (P; p=0.12, t-test). SV diameters were unaltered in the RA/PDA vesicle pool (Q; p=0.06, Mann-Whitney-Wilcoxon test). Box plots show 10, 25, 50, 75 and 90^{th} percentiles with individual data points overlaid. See ***Figure 3—figure supplement 1*** and ***supplementary file 1*** for modified tomogram analysis according to ***Jung et al., 2015a***.
DOI: https://doi.org/10.7554/eLife.29275.007

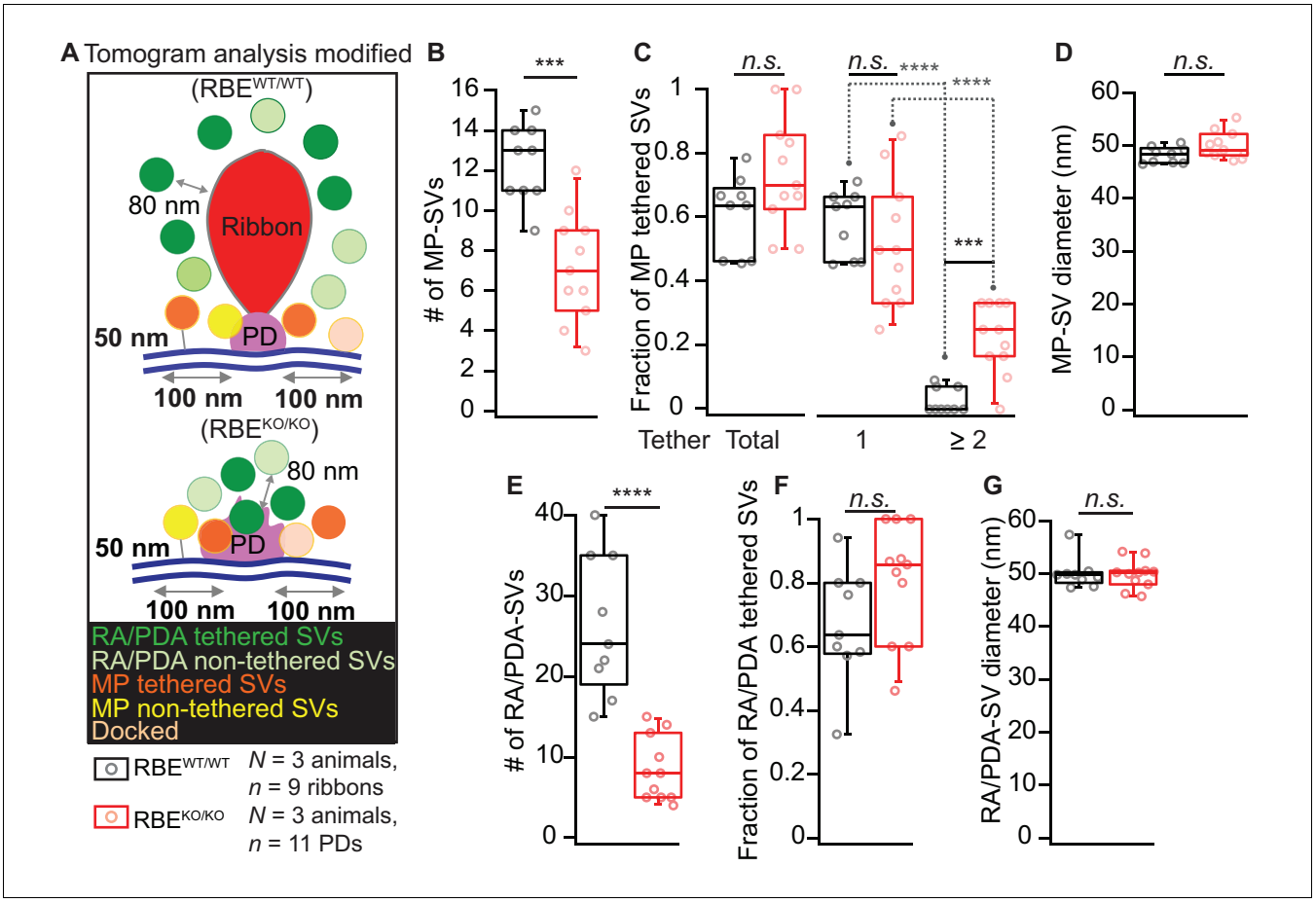

Figure 3—figure supplement 1. Electron tomogram analysis according to ***Jung et al., 2015a***. (**A**) Illustrations for tomogram analysis parameters, as used in ***Jung et al., 2015a*** are depicted. The MP-SVs were defined as vesicles with ≤50 nm from the AZ membrane and with the shortest distance from the vesicle membrane to the presynaptic density of ≤100 nm, excluding the RA/PDA-SVs. (**B–D**) Quantification for MP-SVs: *n* = 11 PDs, N = 3 animals for $RBE^{KO/KO}$ and *n* = 9 ribbons, N = 3 animals for $RBE^{WT/WT}$ were analyzed. Fewer MP-SVs were observed in $RBE^{KO/KO}$ (B; p=0.0001, Mann-Whitney-Wilcoxon test). The fraction of tethered MP-SVs was unaltered in $RBE^{KO/KO}$ (p=0.06, t-test). Most of the SVs were tethered by a single tether in both $RBE^{WT/WT}$ and $RBE^{KO/KO}$. Significantly more multiple-tethered SVs were observed in $RBE^{KO/KO}$ (C; single-tethered MP-SVs; multiple-tethered MP-SVs, *n.s.*: *p*>0.05, ****: p<0.0001, Tukey's test). MP-SV diameters were unaltered in $RBE^{KO/KO}$ (D; p=0.06, Mann-Whitney-Wilcoxon test). (**E–G**) Quantification for RA/PDA-SVs (same sample size): Significantly fewer PDA-SVs were observed in $RBE^{KO/KO}$ than RA-SVs in $RBE^{WT/WT}$ (E; p<0.0001, Mann-Whitney-Wilcoxon test). The fraction of tethered PDA-SVs in $RBE^{KO/KO}$ was comparable to that of tethered RA-SVs in $RBE^{WT/WT}$ (F; p=0.10, t-test). RA/PDA-SV diameters were unaltered (G; p=0.68, Mann-Whitney-Wilcoxon test). Box plots show 10, 25, 50, 75 and 90th percentiles with individual data points overlaid.

DOI: https://doi.org/10.7554/eLife.29275.008

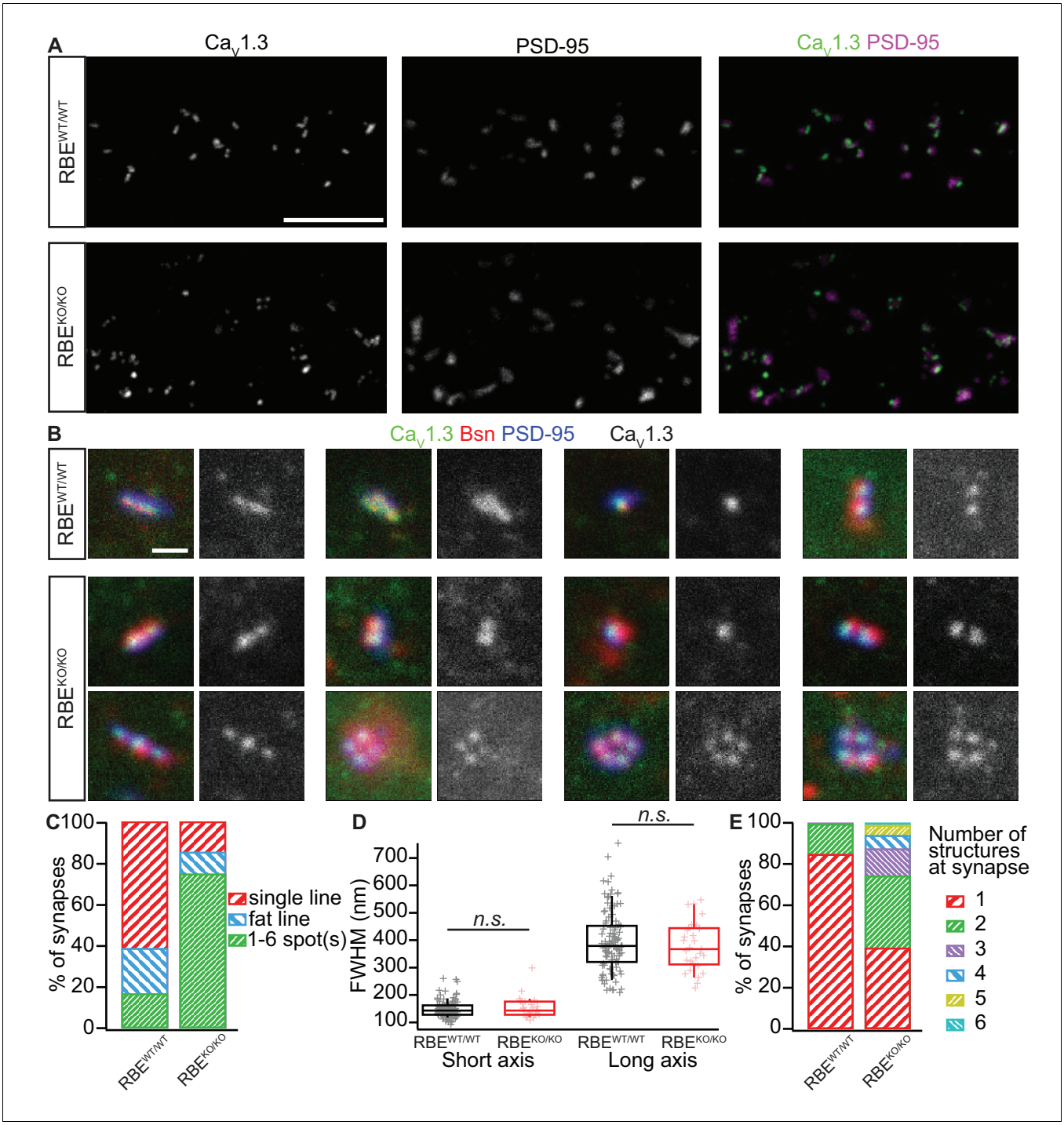

Figure 4. Analyzing AZ Ca^{2+}-channel clusters using confocal and STED immunofluorescence microscopy. (**A**) Maximal projections of confocal sections from organs of Corti immunolabeled for $Ca_V1.3$ Ca^{2+}-channels (left column) and PSD-95 (middle column). The merged pictures (right column) show their juxtaposition in both conditions. While we mostly found one linear/spot-like Ca^{2+}-channel cluster per PSD in $RBE^{WT/WT}$ IHCs (top row), we often observed several spots per PSD in $RBE^{KO/KO}$ IHCs (bottom row). Scale bar = 5 µm. (**B**) Triple co-labeling of $Ca_V1.3$ (green), bassoon (red), and PSD-95 (blue) at several IHC AZs from $RBE^{WT/WT}$ and $RBE^{KO/KO}$ mice, imaged in 2D-STED ($Ca_V1.3$ and PSD-95) and confocal mode (bassoon), showing that $Ca_V1.3$ Ca^{2+}-channels cluster at AZs in IHCs of both genotypes. $Ca_V1.3$ immunofluorescence is displayed in gray next to the merged image for better visualization. Scale bar = 500 nm. (**C**) 178 $RBE^{WT/WT}$ and 183 $RBE^{KO/KO}$ synapses were categorized according to the pattern of $Ca_V1.3$ immunofluorescence found by assigning them to a group of either line-shaped clusters, fat line-shaped clusters or one/multiple spots. A markedly higher fraction of synapses was found to display a spot-like $Ca_V1.3$-signal in $RBE^{KO/KO}$ than in $RBE^{WT/WT}$ IHCs. (**D**) Fitting of a 2D-Gaussian function to the immunofluorescence data of the line-shaped $Ca_V1.3$ clusters showed no difference in terms of size between $RBE^{WT/WT}$ and $RBE^{KO/KO}$ clusters, as

Figure 4 continued on next page

Figure 4 continued

estimated by the full width at half maximum of the Gaussian's short and long axis. Box plots show 10, 25, 50, 75 and 90th percentiles with individual data points overlaid. (**E**) Quantification of the number of fluorescent structures (lines or spots) labeled by the anti-$Ca_V1.3$ antibody at $RBE^{WT/WT}$ and $RBE^{KO/KO}$ synapses showed a significantly increased number in the knockout ($p<0.0001$, Mann-Whitney-Wilcoxon test).

DOI: https://doi.org/10.7554/eLife.29275.009

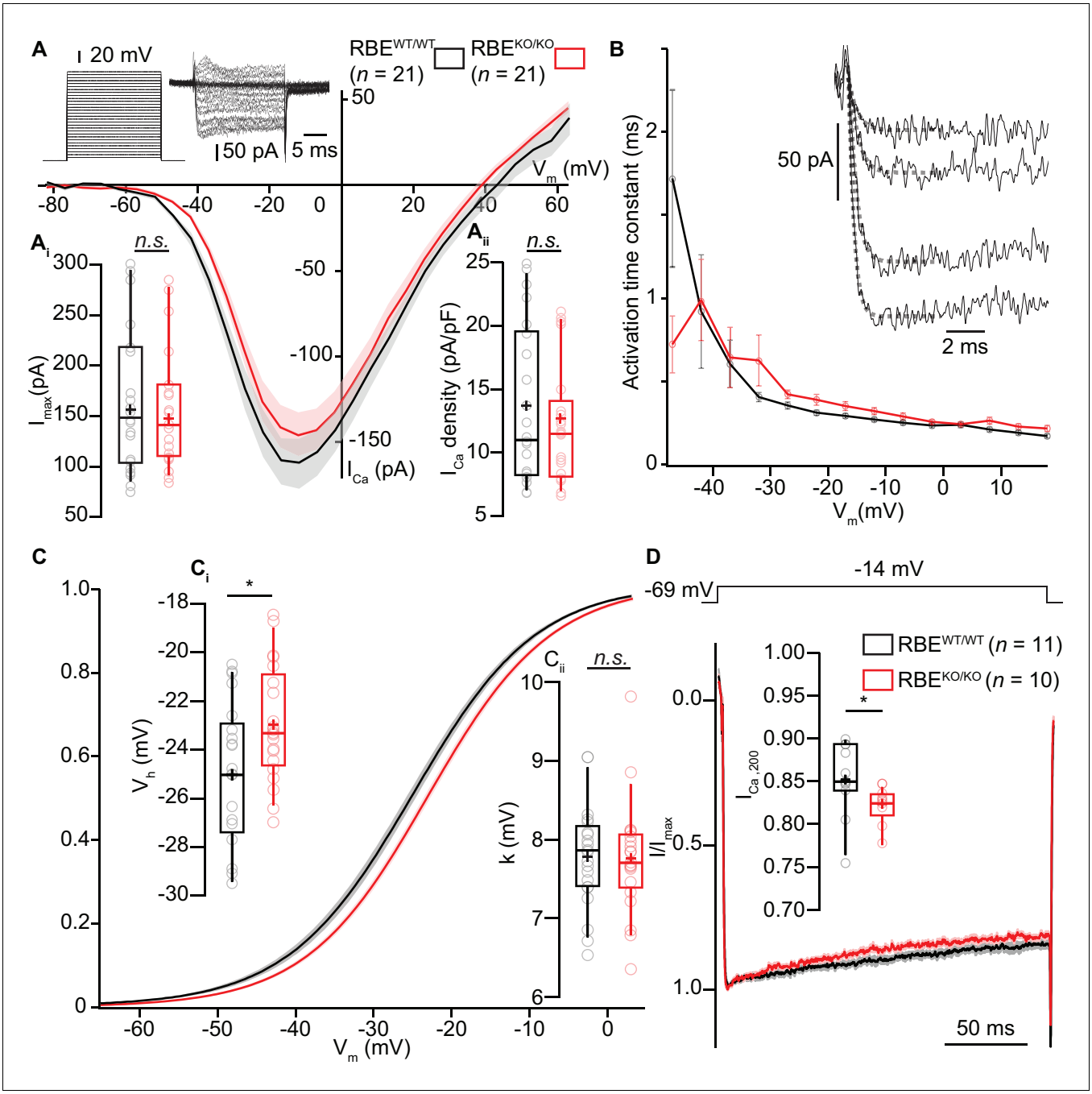

Figure 5. IHC Ca^{2+}-influx shows normal amplitude but a mild depolarized shift in voltage-dependence. (**A**) IV-relationship of the whole-cell Ca^{2+}-current in $RBE^{WT/WT}$ (black, *n* = 21 cells, N = 8) and $RBE^{KO/KO}$ (red, *n* = 21 cells, N = 8) IHCs show comparable (sign-inverted) current amplitudes (**A_i**, p=0.62, t-test) and density (**A_{ii}**, p=0.37, t-test.). Mean (line) ± S.E.M. (shaded areas) are displayed as for (**C, D**). The protocol, consisting of 20 ms steps of 5 mV from −82 to +63 mV, as well as exemplary resulting currents, aredisplayed in the left. Box plots show 10, 25, 50, 75 and 90th percentiles with individual data points overlaid, means are shown as crosses, as for (**C, D**). (**B**) Activation time constants (mean ± S.E.M.) of Ca^{2+}-currents at different potentials were obtained by fitting a power exponential equation to the first 5 ms of the current traces, revealing no differences between conditions. (**C**) Fractional activation of the whole-cell Ca^{2+}-current derived from the IV-relationships (**A**) was fitted to a Boltzmann function. (**Ci**) Box plots of the voltage for half-maximal activation V_h and V_h-estimates of individual IHCs show a depolarized shift of the fractional activation of the $Ca_v1.3$ Ca^{2+}-channels in the $RBE^{KO/KO}$ IHCs (p=0.029, t-test). (**Cii**) Box plots of the voltage-sensitivity or slope factor k and k-estimates of individual IHCs illustrate comparable voltage sensitivity between both conditions (p=0.67, t-test). (**D**) Average peak-normalized Ca^{2+}-currents resulting from 200 ms depolarizations to −14 mV. We observe an enhanced inactivation in ribbonless IHCs, quantified as a reduced residual Ca^{2+}-current (inset). (*n* = 10 cells, N = 5 for $RBE^{KO/KO}$ and *n* = 11 cells, N = 7 in the $RBE^{WT/WT}$; p=0.017, Mann-Whitney-Wilcoxon test).

DOI: https://doi.org/10.7554/eLife.29275.010

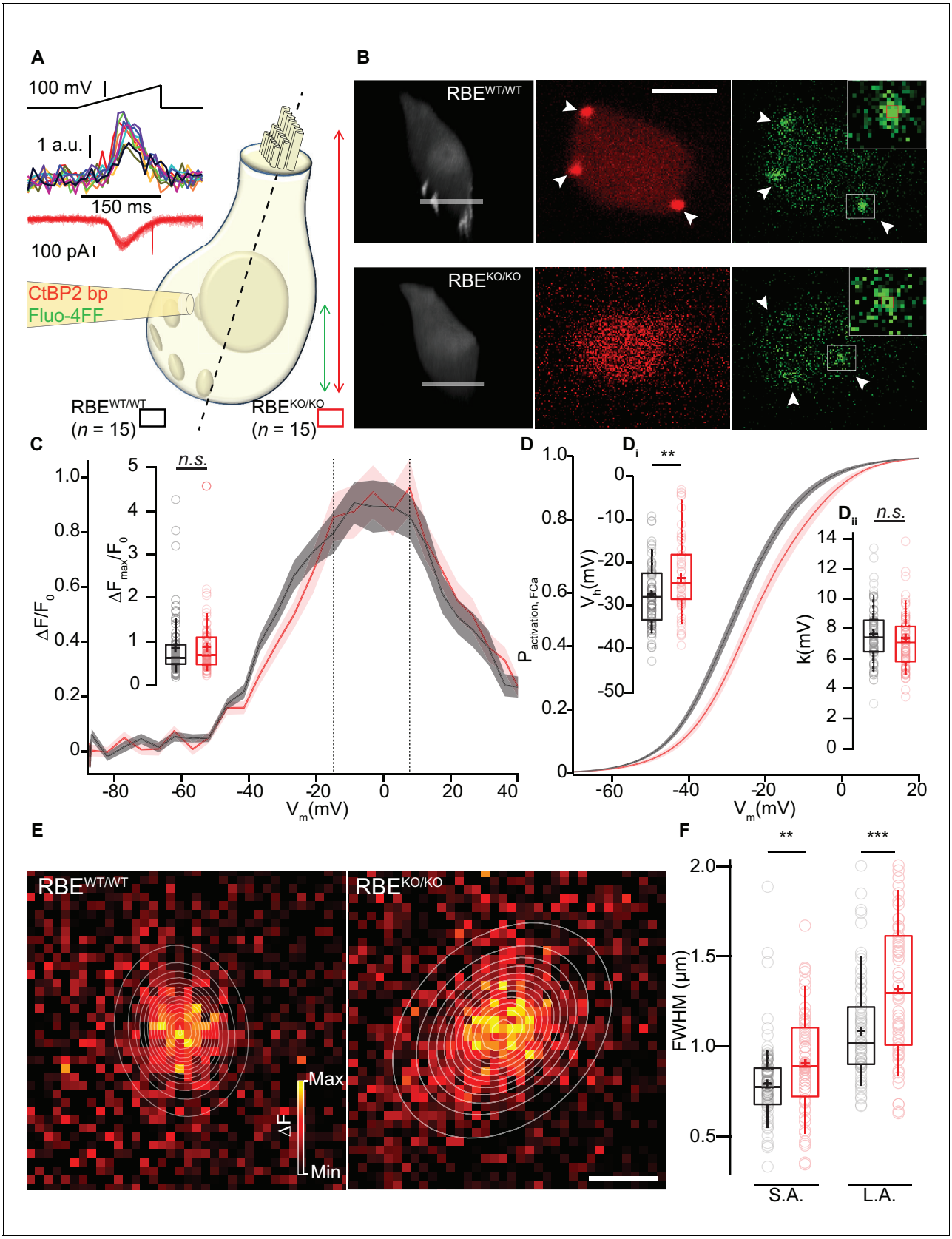

Figure 6. Synaptic Ca^{2+}-influx shows normal amplitude but shifted voltage-dependence and broader spread. (**A, B**) IHCs were patch-clamped at the modiolar basolateral face, loaded with TAMRA-CtBP2-binding peptide and the low affinity Ca^{2+}-indicator Fluo-4FF, and scanned in the red

Figure 6 continued on next page

Figure 6 continued

channel after loading for 4 min to image TAMRA-labeled ribbons, nuclei, and cytosol. 3D projection of TAMRA fluorescence shows the absence of ribbons in $RBE^{KO/KO}$ IHCs (B: 3D projection and red channel). Voltage-ramps from −87 to +63 mV during 150 ms (A: left top) were used to trigger synaptic hotspots of Fluo-4FF fluorescence (A: left middle, 10 AZs in one exemplary $RBE^{WT/WT}$ IHC, B: green channel, marked by arrowheads; ΔF: average of the nine brightest pixels (red square)) and IHC Ca^{2+}-influx (A, left bottom). Ca^{2+}-imaging proceeded from the IHC bottom to the most apical ribbon in $RBE^{WT/WT}$, and from IHC bottom to +12 µm (typically reaching the bottom of nucleus) in $RBE^{KO/KO}$. Scale bar = 5 µm. (**C**) FV-relationship ($\Delta F/F_0$ vs. depolarization level in ramp, protocol as in A): approximating the voltage-dependence of synaptic Ca^{2+}-influx.Mean (line) ± S.E.M. (shaded areas) are displayed as for (**D**). (**Ci**) $\Delta F_{max}/F_0$ was calculated by averaging 5 values at the FV-peak (between the dotted lines) and was comparable between $RBE^{WT/WT}$ (*n* = 78 AZs for 15 cells, N = 8) and $RBE^{KO/KO}$ IHCs (*n* = 61 AZs for 15 cells, N = 7) (p=0.20, Mann-Whitney-Wilcoxon test). Box plots show 10, 25, 50, 75 and 90th percentiles with individual data points overlaid, means are shown as crosses, as for (**D, F**). (**D**) Fractional activation curves derived from fits to the FV-relationships (**C**) were fitted to a Boltzmann function. Mean (line) ± S.E.M. (shaded areas) are displayed. (**Di**) The voltage for half-maximal activation V_h was significantly different between $RBE^{WT/WT}$ (*n* = 68 AZs for 15 IHCs, N = 8) and $RBE^{KO/KO}$ (*n* = 55 AZs for 15 IHCs, N = 7) AZs (p=0.0029, t-test), while the voltage-sensitivity or slope factor k (**Dii**) not (p=0.42, t-test). (**E**) Exemplary ΔF pictures of Fluo-4FF hotspots at $RBE^{WT/WT}$ (left) and $RBE^{KO/KO}$ (right) synapses fitted and overlaid by 2D-Gaussian functions to estimate spatial extent as full width at half maximum (FWHM) for the short axis (S.A.) and the long axis (L.A.). Scale bar = 1 µm. (**F**) Ribbonless synapses of $RBE^{KO/KO}$ IHCs showed a greater spatial spread of the Fluo-4FF fluorescence change. FWHM calculated from the Gaussian fitting to the Fluo-4FF fluorescence hotspot was larger for both axes in $RBE^{KO/KO}$ (*n* = 61 AZs for 15 IHCs, N = 8) compared to $RBE^{WT/WT}$ (*n* = 74 AZs for 15 IHCs, N = 7) (L.A.: p=0.00016; S.A.: p=0.0029, t-test).

DOI: https://doi.org/10.7554/eLife.29275.011

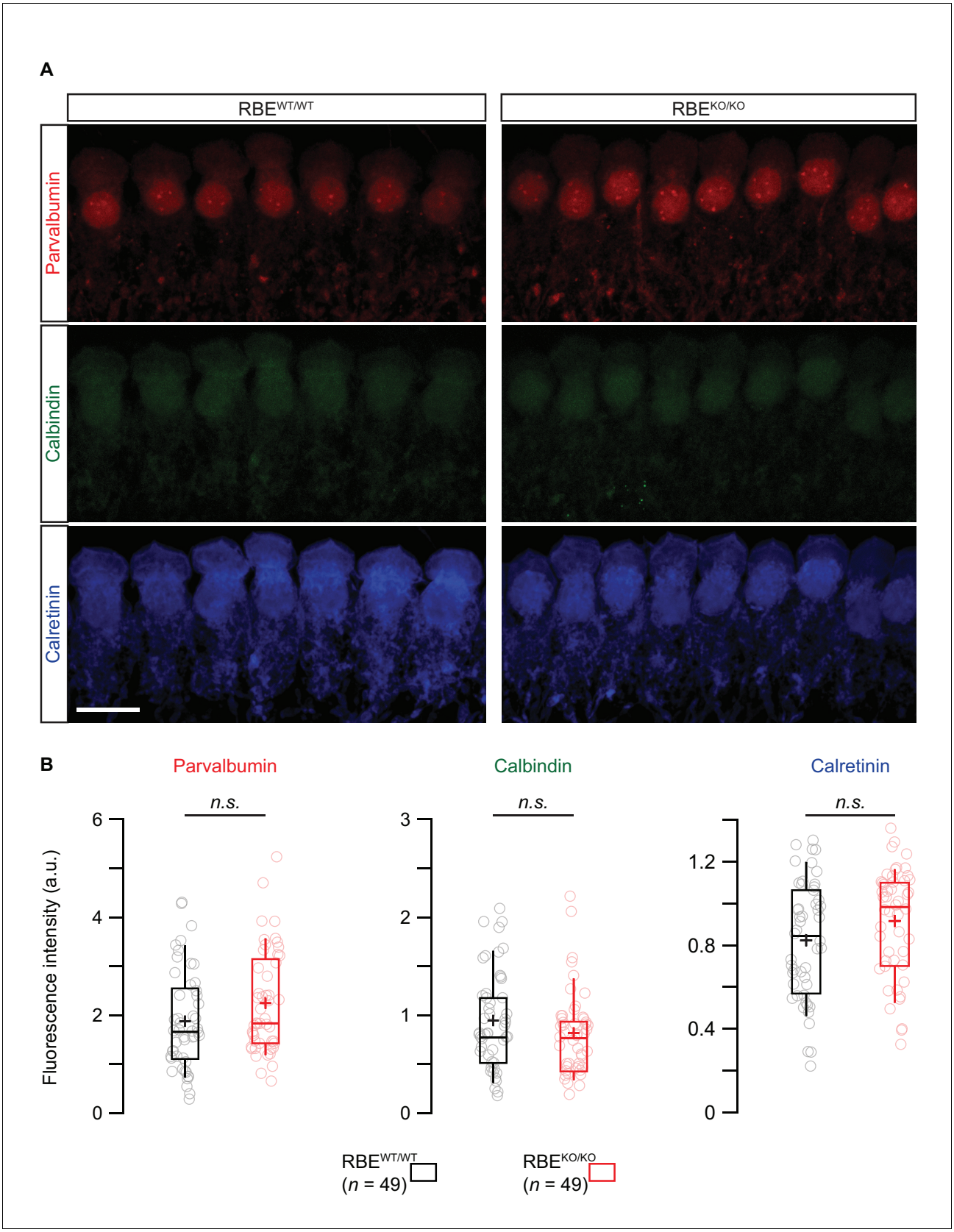

Figure 6—figure supplement 1. Semi-quantitative immunofluorescence analysis of the three main proteinaceous Ca^{2+}-buffers. (**A**) Maximal projection of confocal sections from organs of Corti co-immunolabeled for parvalbumin (top row), calbindin (middle row) and calretinin (bottom row). Scale

Figure 6—figure supplement 1 continued on next page

Figure 6—figure supplement 1 continued

bar = 10 µm. (**B**) Box plots showed no significant differences in immunofluorescence intensities for the three proteinaceous Ca^{2+}-buffers between $RBE^{KO/KO}$ and $RBE^{WT/WT}$ conditions (*n* = 49 IHCs, N = 4 for both genotypes, p=0.08, 0.23 and 0.09 from left to right, Mann-Whitney-Wilcoxon test for all). Box plots show 10, 25, 50, 75 and 90^{th} percentiles with individual cells overlaid; means are shown as crosses.

DOI: https://doi.org/10.7554/eLife.29275.012

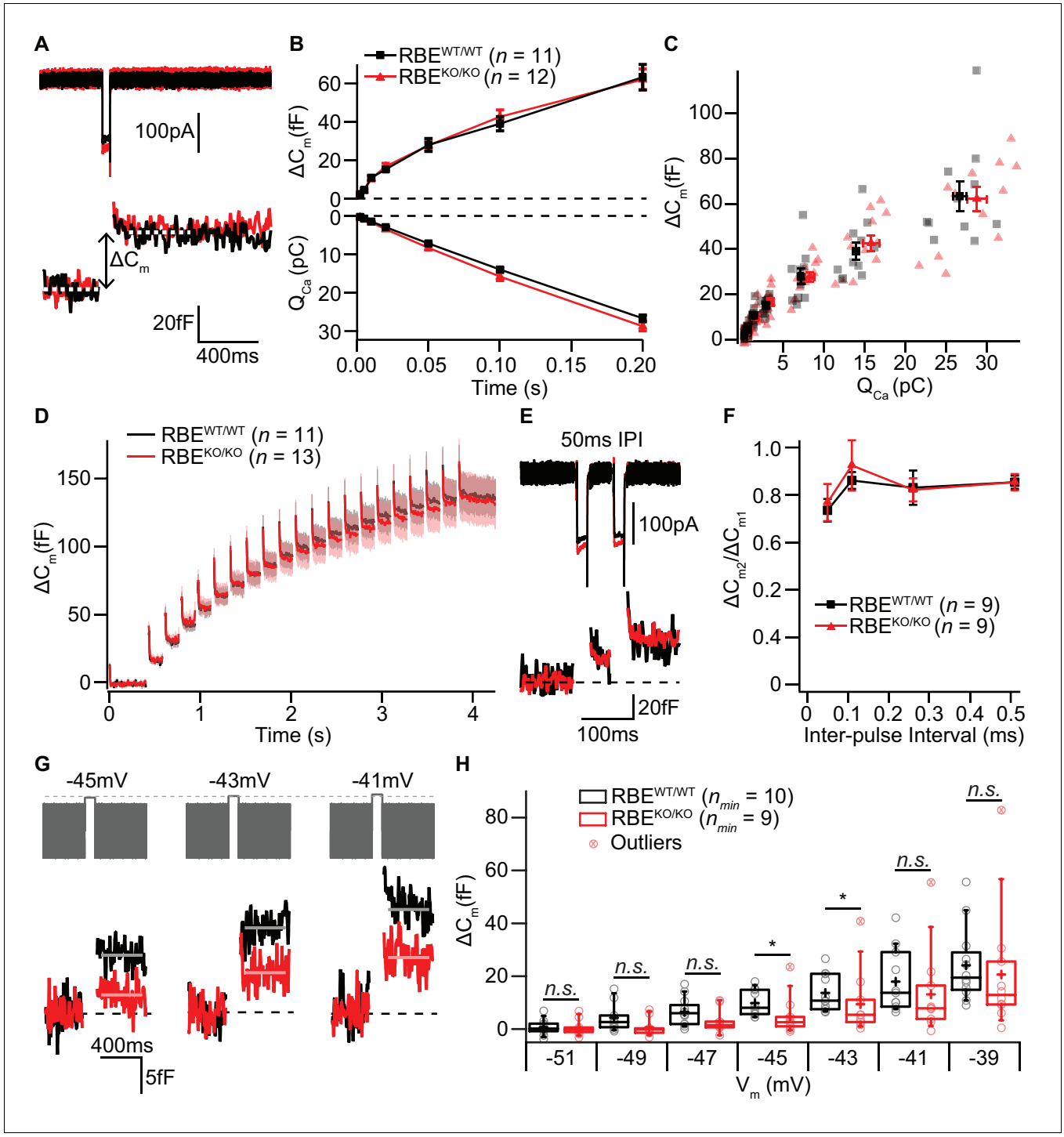

Figure 7. IHC exocytosis is normal for strong depolarizations but mildly reduced for weak ones. (**A**) Representative Ca^{2+}-currents (top) and corresponding low passed-filtered membrane capacitance (ΔC_m) traces recorded from $RBE^{WT/WT}$ and $RBE^{KO/KO}$ IHCs upon 50 ms depolarizations from −69 to −14 mV. (**B**) Cumulative exocytosis (exocytic ΔC_m, top) and corresponding Ca^{2+}-charge (Q_{Ca}, bottom) of $RBE^{WT/WT}$ (n = 11 cells, N = 8) and $RBE^{KO/KO}$ (n = 12 cells, N = 7) IHCs as a function of stimulus duration (2 to 200 ms to −14 mV) were unaltered in $RBE^{KO/KO}$ IHCs. Data is presented as mean ± S.E.M as for (**F**). (**C**) Relating ΔC_m to the corresponding Q_{Ca} indicated comparable Ca^{2+} efficiency of exocytosis between $RBE^{WT/WT}$ and $RBE^{KO/KO}$ IHCs. Mean ± S.E.M. for each pulse duration is presented in black and red; individual IHCs data points are overlaid. (**D**) Mean ΔC_m traces (shaded areas: S.E.M.) in response to trains of 20 ms depolarizations from −87 to −17 mV (20 stimuli separated by 160 ms) of $RBE^{WT/WT}$ (n = 11 cells, N = 5) and $RBE^{KO/KO}$ (n = 13 cells, N = 8) IHCs show comparable exocytic ΔC_m. (**E**) Representative low pass-filtered ΔC_m traces in response to a pair of 20 ms pulses to −17 mV, separated by a 50 ms of inter-pulse interval (IPI). (**F**) Ratios of exocytosis ($\Delta C_{m2}/\Delta C_{m1}$) to a pair of 20 ms pulses with varying inter-

Figure 7 continued on next page

Figure 7 continued

pulse intervals (50, 110, 260 and 510 ms) reveal a comparable recovery from RRP depletion between $RBE^{WT/WT}$ (n = 9 cells, N = 6) and $RBE^{KO/KO}$ IHCs (n = 9 cells, N = 6). (**G**) Representative low pass-filtered ΔC_m traces in response to 100 ms step-depolarizations to −45, –43 and −41 mV. (**H**) Box plot and single values of ΔC_m elicited by 100 ms step-depolarizations of $RBE^{WT/WT}$ (n_{min} = 10 cells, N = 8) and $RBE^{KO/KO}$ (n_{min} = 9 cells, N = 9) IHCs to different potentials. Exocytic ΔC_m of $RBE^{KO/KO}$ IHCs was reduced for mild depolarizations (−45, –43 and −41 mV; p=0.0115, p=0.0295 and p=0.1321, respectively; p=0.0017, p=0.0042 and p=0.0489, without definitive outliers; Mann-Whitney-Wilcoxon test), but comparable to $RBE^{WT/WT}$ IHCs at stronger depolarizations (−39 mV; p=0.2030, Mann-Whitney-Wilcoxon test). Box plots show 10, 25, 50, 75 and 90th percentiles with the individual data points overlaid.

DOI: https://doi.org/10.7554/eLife.29275.013

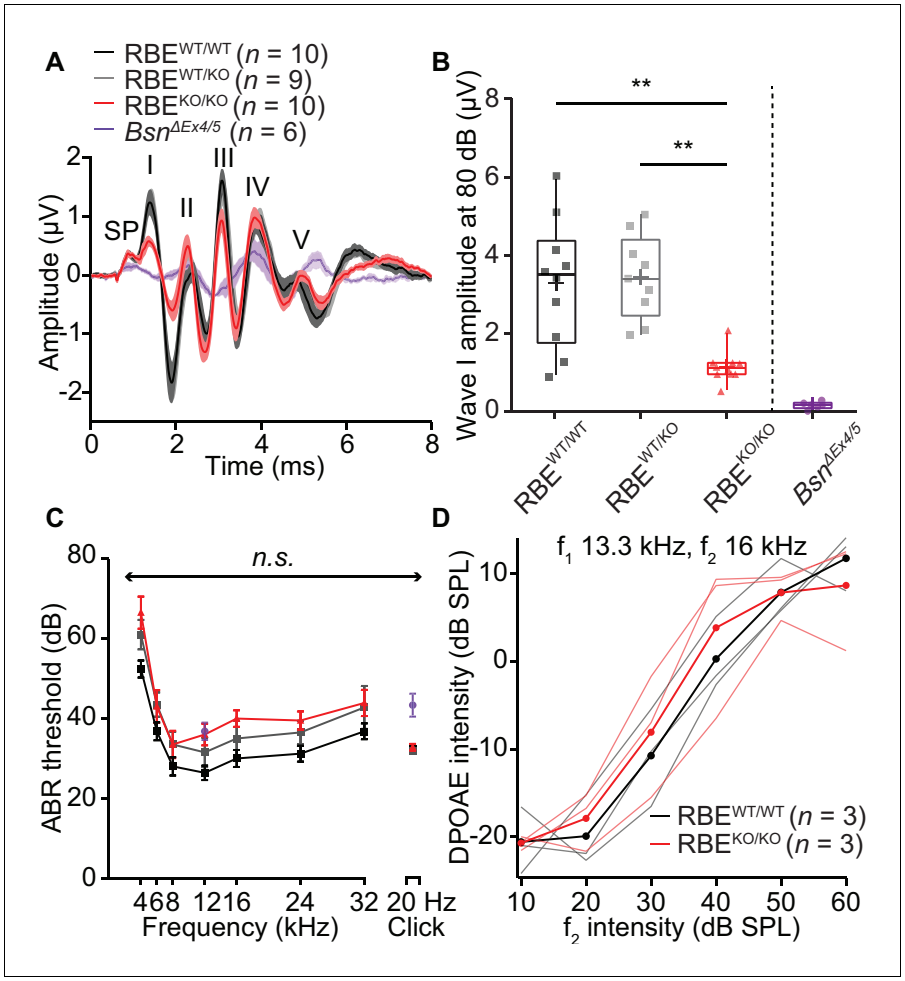

Figure 8. Auditory brainstem responses indicate impaired synchronous SGN activation in RBE$^{KO/KO}$ mice. (**A**) Average ABR waveforms in response to 80 dB clicks (n = N = 10 for RBE$^{KO/KO}$ and RBE$^{WT/WT}$, N = 9 for RBE$^{WT/KO}$ at 6 weeks of age) showed a reduced amplitude of ABR wave I in RBE$^{KO/KO}$ mice indicating an impairment of SGN activation, which is quantified in (**B**). This decrease was not as pronounced as in SGNs lacking bassoon (*Bsn*$^{\Delta Ex4/5}$, data from ***Jing et al., 2013***). The central ABR waves were better preserved, except for wave III. SP: summating potential (hair cell receptor potential), roman numerals (**I–V**): ABR waves generated along the early auditory pathway. Mean (lines) ± S.E.M. (shaded areas) are displayed. (**B**) ABR wave I was significantly reduced in RBE$^{KO/KO}$ mice as compared to RBE$^{WT/WT}$ and RBE$^{WT/KO}$ (p=0.0051 and p=0.0017, respectively, NPMC test). No statistical significance was observed between responses recorded in RBE$^{WT/WT}$ and RBE$^{WT/KO}$ mice (p>0.9999, NPMC test). Data from *Bsn*$^{\Delta Ex4/5}$ are shown for comparison. Box plots show 10, 25, 50, 75 and 90th percentiles with the individual data points overlaid, means are shown as crosses. (**C**) ABR thresholds were comparable in RBE$^{WT/WT}$, RBE$^{WT/KO}$ and RBE$^{KO/KO}$ for tone burst-driven (*n.s.*, Tukey's test) and click-driven ABRs (*n.s.*, NPMC test). Previously published data for *Bsn*$^{\Delta Ex4/5}$ showed elevated thresholds as a response to short stimuli (click 20 Hz) but a similar threshold level at 12 kHz. (**D**) DPOAE amplitude in response to pairs of simultaneous sine waves (f_1 and f_2, frequencies indicated on panel) at increasing stimulus intensity (f_1 intensity 10 dB above f_2 in all cases). Mean (thick lines) and data from individual mice (n = N = 3 in RBE$^{WT/WT}$ and RBE$^{KO/KO}$) are displayed.

DOI: https://doi.org/10.7554/eLife.29275.014

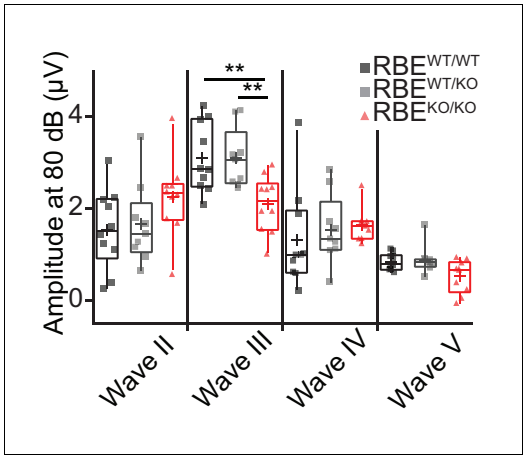

Figure 8—figure supplement 1. Quantification of ABR waves II-V amplitude in $RBE^{KO/KO}$ mice. Mean ABR wave II-V amplitude in response to an 80 dB click in 6/8 week-old mice. Responses were comparable in waves II, IV and V (Tukey's test for comparison of the three groups regarding wave II and III, NPCM test for comparison of wave IV and V, n = N = 10 for $RBE^{WT/WT}$ and $RBE^{KO/KO}$, n = N = 9 for $RBE^{WT/KO}$), but significantly reduced in wave III in $RBE^{KO/KO}$ mice as compared to $RBE^{WT/WT}$ and $RBE^{WT/KO}$ (p=0.0093 and p=0.0075, respectively). Box plots show 10, 25, 50, 75 and 90th percentiles with individual data points overlaid and means are shown as crosses.

DOI: https://doi.org/10.7554/eLife.29275.015

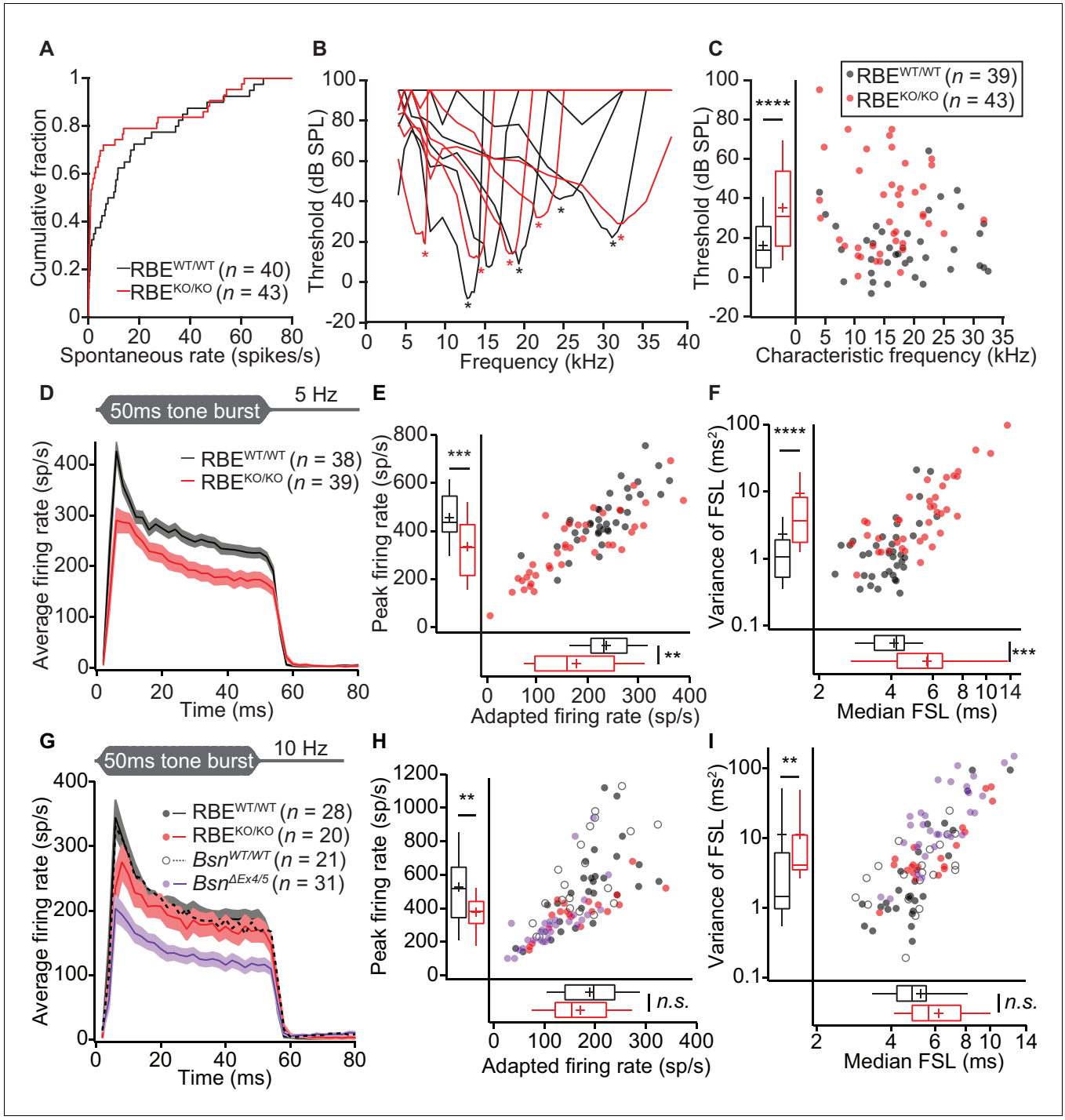

Figure 9. Impaired spontaneous and sound-evoked firing in putative SGNs of RBE$^{KO/KO}$ mice. (**A**) Cumulative distribution functions of spontaneous firing rates of putative SGNs showed a higher fraction of low spontaneous rate SGNs in RBE$^{KO/KO}$ mice (n = 43 SGNs) than in RBE$^{WT/WT}$ mice (n = 40 SGNs, N = 8) (p=0.027, Kolmogorov-Smirnov test). (**B**) Representative frequency tuning curves of RBE$^{KO/KO}$ and RBE$^{WT/WT}$ SGNs showed comparable sharpness of tuning between SGNs of both genotypes. * point to the characteristic frequency (C_f) for which an increase in SGN firing requires the least sound pressure level. (**C**) Thresholds at C_f of RBE$^{KO/KO}$ SGNs (n = 43 SGNs, N = 9) were higher than those in RBE$^{WT/WT}$ mice (n = 39 SGNs, N = 9) (p<0.0001, Mann-Whitney-Wilcoxon test). Box plots show 10, 25, 50, 75 and 90th percentiles, means are shown as crosses, as for (**E**), (**F**), (**H**) and (**I**). (**D**) Average PSTH (bin width = 2 ms) of RBE$^{KO/KO}$ (n = 39 SGNs, N = 8) and RBE$^{WT/WT}$ SGNs (n = 38 SGNs, N = 9) recorded in response to 50 ms tone bursts at C_f 30 dB above threshold at a stimulus rate of 5 Hz. The time course of adaptation of RBE$^{KO/KO}$ SGNs (calculated by fitting a single exponential function to the individual histograms) was significantly longer (p=0.033, Mann-Whitney-Wilcoxon test). Mean (line) ± S.E.M. (shaded areas) are displayed as for (**G**). (**E**) Scatterplot of peak firing rate (bin with highest rate at sound onset) and adapted firing rate (averaged 35–45 ms from

Figure 9 continued on next page

Figure 9 continued

response onset) revealed lower firing rates in $RBE^{KO/KO}$ (n = 39 SGNs) as compared to $RBE^{WT/WT}$ (n = 38 SGNs, N = 9) mice (data from (**D**), peak rate: p=0.0001, adapted rate: p=0.0023, Mann-Whitney-Wilcoxon test). (**F**) Increased latency (data from (**D**), p=0.0002) and variance of latency (p<0.0001, Mann-Whitney-Wilcoxon test) of the first spike after sound onset in $RBE^{KO/KO}$ SGNs indicated lower temporal precision of sound onset coding. (**G**) Average PSTH (bin width = 2 ms) of $RBE^{KO/KO}$ (n = 20 SGNs, N = 6) and $RBE^{WT/WT}$ SGNs (n = 28 SGNs, N = 8) were recorded in response to 50 ms tone bursts at C_f 30 dB above threshold at a stimulus rate of 10 Hz and showed a similar adapted response in $RBE^{KO/KO}$ as compared to lower stimulation rates (***Figures 9,11***) but still a lower onset response than in $RBE^{WT/WT}$ SGNs. Responses in $Bsn^{\Delta Ex4/5}$ mutants (shown for comparison, re-plotted from ***Jing et al., 2013***) were considerably lower. (**H**) Scatterplot of peak firing rate (bin with highest rate at sound onset) and adapted firing rate (averaged 35–45 ms from response onset) show decreased onset firing rates in $RBE^{KO/KO}$ as compared to $RBE^{WT/WT}$ mice (data from (**G**), p=0.0093, Mann-Whitney-Wilcoxon test). The adapted response was comparable in both cases (p=0.3584, t-test). Data points from $Bsn^{\Delta Ex4/5}$ mutants (re-plotted from ***Jing et al., 2013***) and WT littermates are shown for comparison, also in (**I**). (**I**) Increased variance of first spike latency after sound onset in $RBE^{KO/KO}$ SGNs (p=0.0089, Mann-Whitney-Wilcoxon test) and comparable latencies were observed at this stimulation frequency (data from (**G**), p=0.0761, Mann-Whitney-Wilcoxon test).

DOI: https://doi.org/10.7554/eLife.29275.016

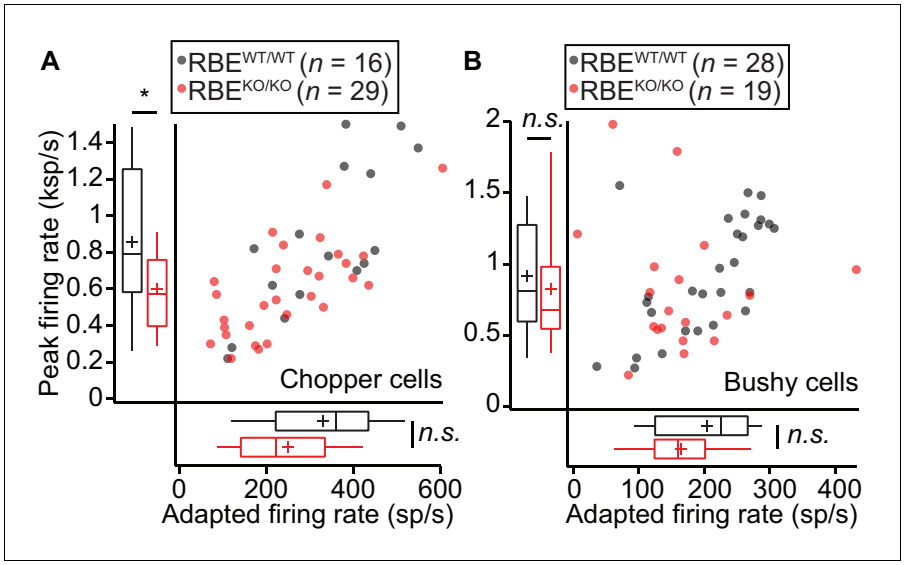

Figure 10. Responses to pure tones in cochlear nucleus cells showed that the mutant phenotype is partially compensated in higher stations of the auditory pathway. (**A**) Quantification of peak and adapted responses to 50 ms tone burst stimulation, 30 dB above threshold at C_f in SGNs displaying a chopper discharge pattern (periodically alternating phases of high firing rates with low firing rates, typical of multipolar cells in the posterior ventral cochlear nucleus), showed that the differences in rate faded away opposite to those shown at the level of the auditory nerve. Peak rates were still significantly lower in $RBE^{KO/KO}$ (n = 29 SGNs, N = 9) as compared to $RBE^{WT/WT}$ (n = 16 SGNs, N = 9) mice (p=0.0303, Mann-Whitney-Wilcoxon test), while the adapted rate showed a non-significant trend towards reduction in $RBE^{KO/KO}$ (p=0.0538, t-test). Box plots show 10, 25, 50, 75 and 90th percentiles and means are shown as crosses, as for (**B**). (**B**) Same recordings paradigm as (**A**) performed in a fiber with bushy cell discharge pattern (similar to the one found in SGNs, typical also in this type of cochlear nucleus neurons) showed comparable responses in both peak (p=0.2601, Mann-Whitney-Wilcoxon test) and adapted rate (p=0.0510, Mann-Whitney-Wilcoxon test) in $RBE^{KO/KO}$ (n = 19 SGNs, N = 7) and $RBE^{WT/WT}$ (n = 28 SGNs, N = 10).
DOI: https://doi.org/10.7554/eLife.29275.017

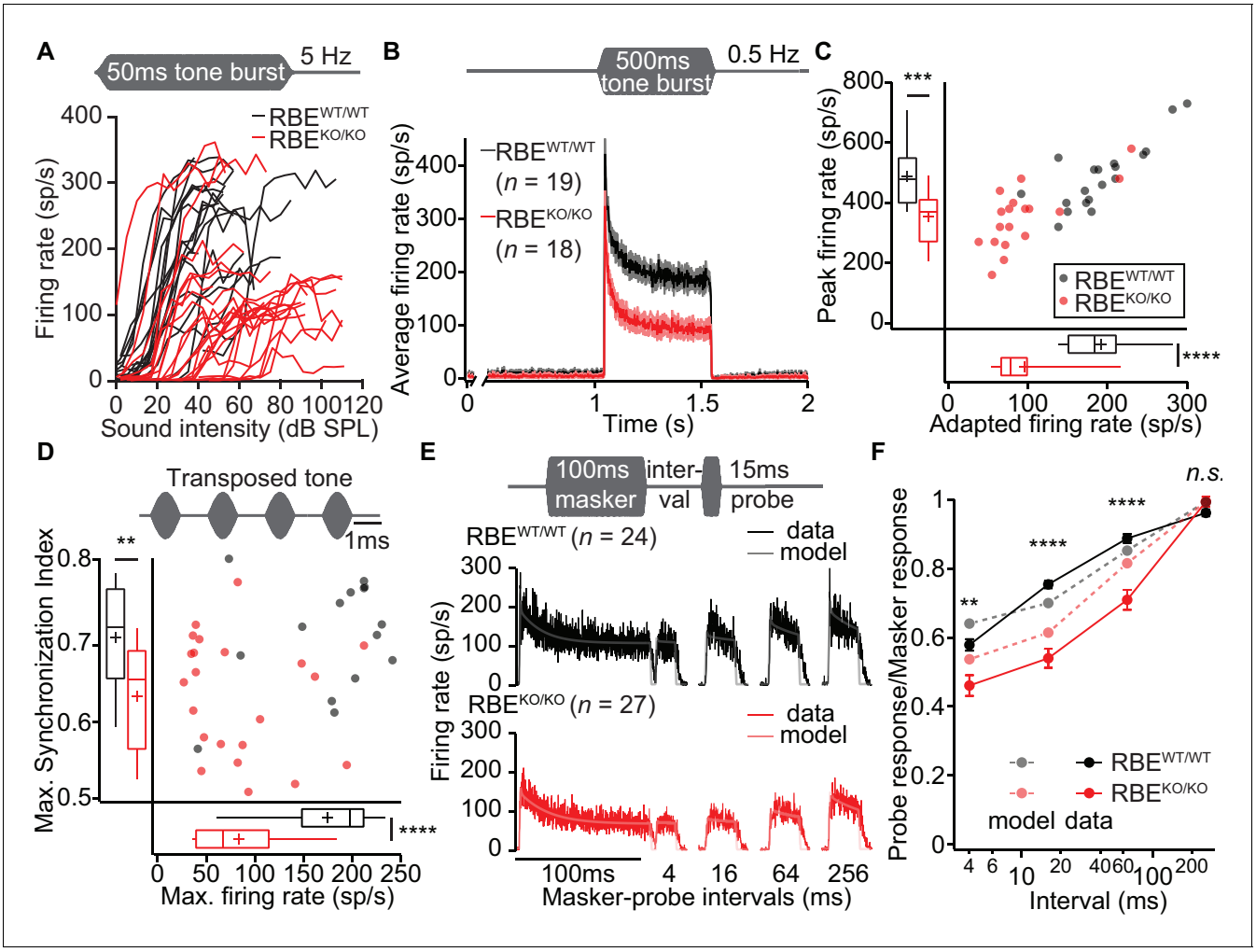

Figure 11. Lack of ribbons impairs vesicle replenishment in RBE$^{KO/KO}$ mice. (**A**) Intensity coding was largely preserved for suprathreshold sound stimulation: rate-level functions (average increase in spike rate with stimulus intensity) of SGNs in response to 50 ms tone bursts at C_f at 5 Hz corroborated the notion of increased sound threshold but were otherwise comparable in RBE$^{KO/KO}$ (n = 24 SGNs, N = 8) and RBE$^{WT/WT}$ (n = 19 SGNs, N = 7) mice, for quantification see ***Figure 11—figure supplement 1C***. (**B**) Average PSTH recorded in response to 50 × 500 ms tone bursts at C_f and 30 dB above threshold at a stimulus rate of 0.5 Hz (bin width = 2 ms): the onset response to this stimulus was preserved better in RBE$^{KO/KO}$ SGNs (n = 18 SGNs, N = 7) as compared to higher stimulation rates (***Figure 9***), but it was still lower than in RBE$^{WT/WT}$ SGNs (n = 19 SGNs, N = 7), as well as the adapted firing rate. Mean (line) ± S.E.M. (shaded areas) are displayed. (**C**) Scatterplot of peak (highest 2 ms bin) and adapted (averaged 405–415 ms from response onset) firing rates: significantly reduced peak (p=0.0005, t-test) and adapted (p<0.0001, Mann-Whitney-Wilcoxon test) rates in RBE$^{KO/KO}$ SGNs. Box plots show 10, 25, 50, 75 and 90th percentiles and means are shown as crosses, as for (**D**). (**D**) Temporal precision and reliability of sound coding is impaired in RBE$^{KO/KO}$ SGNs. Synchronization of firing to stimulus and firing rates (reflecting spike probability) were reduced when probed with amplitude-modulated (transposed) tones (continuous stimulation with a carrier frequency at C_f and at a modulation frequency of 500 Hz) (p=0.0043, t-test, for synchronization index, and p<0.0001, t-test, for firing rate, when comparing RBE$^{KO/KO}$ (n = 22 SGNs, N = 7) and RBE$^{WT/WT}$ (n = 15 SGNs, N = 6) SGNs). (**E**) Forward masking experiments were used to study presynaptic SV dynamics: a stimulus complex consisting of a 100 ms masker stimulus, a silent interval of 4/16/64/256 ms and a 15 ms probe (both at the characteristic frequency, 30 dB above threshold) was presented at 2 Hz. The averaged data after alignment of RBE$^{WT/WT}$ (n = 24 SGNs, N = 7, black) and RBE$^{KO/KO}$ (n = 27 SGNs, N = 8, red) SGNs responses are displayed as described in Materials and methods. On top of the data we present a fit of a biophysical model (light gray and pink lines) to the data used to study the SV dynamics at the AZ. The refilling and fusion rate constant during spontaneous and stimulated conditions as well as the number of occupied release sites are provided in ***Table 2***. (**F**) Recovery of onset response showed as ratio of probe and masker response (number of spikes during first 10 ms, mean ± S.E.M), and prediction (dashed lines) derived from the model fit shown in (**E**). Recovery was slower in RBE$^{KO/KO}$ SGNs (n = 27 SGNs, N = 8) as compared to RBE$^{WT/WT}$ (n = 24 SGNs, N = 7) with significant differences in the ratio after 4 ms (p=0.0019, t-test), 16 ms (p<0.0001, Mann-Whitney-Wilcoxon test), and 64 ms masker-probe intervals (p<0.0001, Mann-Whitney-Wilcoxon test), but not after 256 ms (p=0.0835, t-test).

DOI: https://doi.org/10.7554/eLife.29275.019

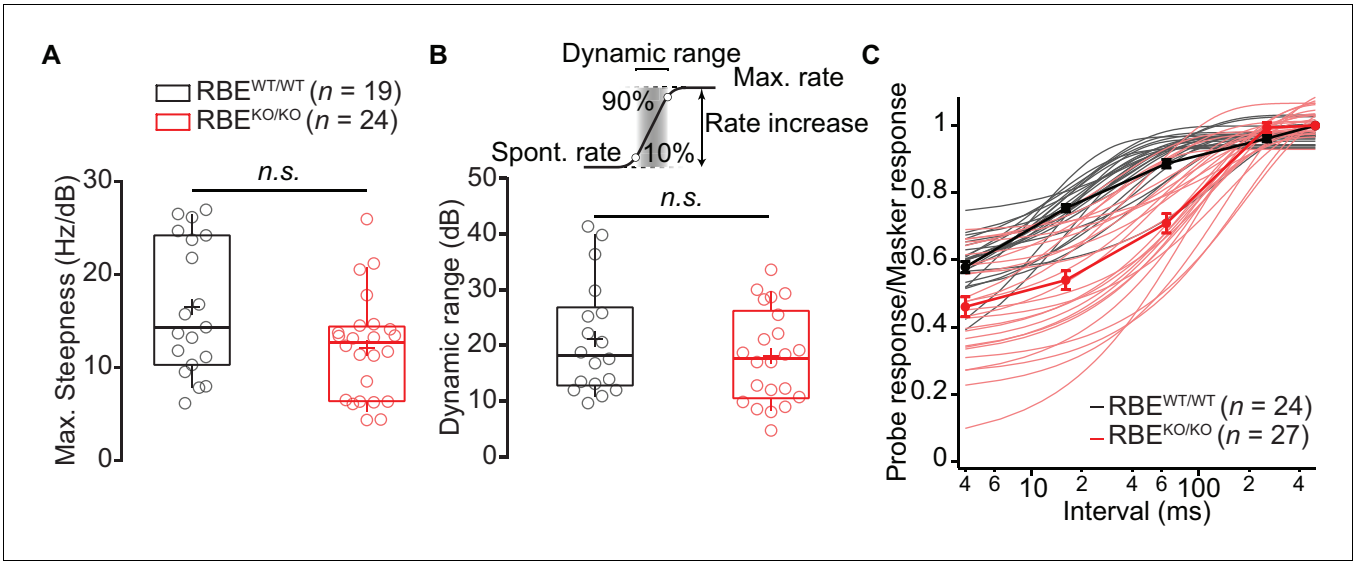

Figure 11—figure supplement 1. Rate-level functions and dynamic range remained unchanged in $RBE^{KO/KO}$. (**A**) Maximal steepness of the rate-level functions (average increase of spike rate with sound intensity) were comparable in $RBE^{KO/KO}$ (*n* = 24 SGNs, N = 8) and $RBE^{WT/WT}$ (*n* = 19 SGNs, N = 7) (p=0.0679, Mann-Whitney-Wilcoxon test). Box plots show 10, 25, 50, 75 and 90th percentiles and means are shown as crosses, as for (**B**). (**B**) Dynamic range is defined as the range of sound intensity levels in which the rate–level function shows a spike rate increase between 10% and 90% of the difference between spontaneous and maximal rate. The absence of ribbon in $RBE^{KO/KO}$ did not affect this estimate significantly (p=0.3044, t-test). (**C**) Ratio of probe and masker onset response (number of spikes during first 10 ms, mean ± S.E.M.) and single exponential fits to individual units ($RBE^{KO/KO}$, *n* = 27 SGNs, N = 8, pink and $RBE^{WT/WT}$, *n* = 24 SGNs, N = 7, gray) showed a slower recovery in $RBE^{KO/KO}$ with a significantly lower time constant (p<0.0001, Mann-Whitney-Wilcoxon test).

DOI: https://doi.org/10.7554/eLife.29275.020